NASA/TM—20220004659

# Multi-Fidelity CFD Simulation of the Multirotor Test Bed

*Jasim Ahmad, Sarah Conley, Carl Russell*
*Ames Research Center, Moffett Field, California*

# Table of Content

# NASA STI Program ... in Profile

Since its founding, NASA has been dedicated to the advancement of aeronautics and space science. The NASA scientific and technical

- CONFERENCE PUBLICATION. Collected papers from scientific and technical conferences, symposia, seminars,

information (STI) program plays a key part in helping NASA maintain this important role.

The NASA STI program operates under the auspices of the Agency Chief Information Officer. It collects, organizes, provides for archiving, and disseminates NASA's STI. The NASA STI program provides access to the NASA Aeronautics and Space Database and its public interface, the NASA Technical Reports Server, thus providing one of the largest collections of aeronautical and space science STI in the world. Results are published in both non-NASA channels and by NASA in the NASA STI Report Series, which includes the following report types:

- TECHNICAL PUBLICATION. Reports of completed research or a major significant phase of research that present the results of NASA Programs and include extensive data or theoretical analysis. Includes compila- tions of significant scientific and technical data and information deemed to be of continuing reference value. NASA counter- part of peer-reviewed formal professional papers but has less stringent limitations on manuscript length and extent of graphic presentations.

- TECHNICAL MEMORANDUM. Scientific and technical findings that are preliminary or of specialized interest, e.g., quick release reports, working papers, and bibliographies that contain minimal annotation. Does not contain extensive analysis.

- CONTRACTOR REPORT. Scientific and technical findings by NASA-sponsored contractors and grantees.

or other meetings sponsored or co-sponsored by NASA.

- SPECIAL PUBLICATION. Scientific, technical, or historical information from NASA programs, projects, and missions, often concerned with subjects having substantial public interest.

- TECHNICAL TRANSLATION. English-language translations of foreign scientific and technical material pertinent to NASA's mission.

Specialized services also include organizing and publishing research results, distributing specialized research announcements and feeds, providing information desk and personal search support, and enabling data exchange services.

For more information about the NASA STI program, see the following:

- Access the NASA STI program home page at http://www.sti.nasa.gov

- E-mail your question to help@sti.nasa.gov

- Fax your question to the NASA STI Information Desk at 443-757-5803

- Phone the NASA STI Information Desk at 443-757-5802

- Write to:
  STI Information Desk
  NASA Center for AeroSpace Information
  7115 Standard Drive
  Hanover, MD 21076-1320

This report is also available in electronic form at

http://www.nas.nasa.gov/publications/reports/reports.html

**Abstract**

The high-fidelity and reduced order CFD method's validation and analysis are presented for the Multirotor Test Bed. The reduced-order method uses a rotor-disk model in the OVERFLOW CFD code and is an important aspect of this study. A rotor-trim option loosely coupling the comprehensive code CAMRAD II with the OVERFLOW CFD code is included in the simulation that captures rotor blade aerodynamics, blade and rotor performance, rotor-rotor, and rotor-body interactions. Detailed comparison and validation were performed for both higher-fidelity full rotor unsteady flows and reduced-order rotor-disk methods. The tunnel geometry is included in the detailed computational effort. Computations of the low-Reynolds number flows were performed for a different number of in-plane rotors as well as for a single rotor modeled inside the tunnel.

Introduction

NASA recently developed the Multirotor Test Bed (MTB) [ref. 1-3] system as a part of the agency's Revolutionary Vertical Lift Technology (RVLT) Project to facilitate wind tunnel testing for new and existing multirotor aircraft configurations, with a focus on collecting validation data for Urban Air Mobility (UAM) vehicle simulations. The MTB is currently capable of testing up to six rotors with the potential to expand to more than six rotors. The MTB is designed to adjust the vertical, lateral, and longitudinal placement of each rotor, as well adjust the rotor tilt and the pitch of the whole assembly. Improvements are currently being made to the MTB to improve the quality of the data measurements for future MTB testing scheduled for testing in 2022.

Conventional helicopter flow fields are complex in general and multirotor UAM aircraft system flow fields are even more complex and require high-fidelity Navier-Stokes simulations for accurate representation. The knowledge gained from conventional helicopter flow fields is useful for understanding the low Reynolds number flow about UAM vehicles but is not directly applicable due to the large variations of the flow field Reynolds number and the interaction of the rotor flow filed with support structures. The flow field, whether in forward flight or hover, consists of unsteady aerodynamics with complex three-dimensional wakes dominated by the blade tip vortices. The wake also contains shear layers that are produced as the turbulent boundary layers detach from the blade surface. As the tip vortices convect away from the rotor blade, the vortex cores entrain part of the shear layer, and as such, the flow is inherently unsteady. To capture the rotor blade aerodynamic-structural interactions, high-fidelity Computational Fluid Dynamics (CFD), and Computational Structural Dynamics (CSD) analyses are coupled to accurately model the flow field, rotor blade motion, and rotor trim. The computational simulation of such unsteady, moving, and often deforming surfaces, is time-consuming, difficult, and not computationally expensive. Recently, there has been increased interest in the aerodynamics of multirotor vehicles such as those proposed for the emerging UAM market; vehicle geometries include quadcopters, side-by-side rotors, and lift plus cruise configurations. Modeling these multirotor configurations requires increased computational effort. The OVERFLOW simulation captures rotor blade aerodynamics, blade, and rotor performance, and rotor-body interactions to improve understanding and performance of multirotor systems. Besides a higher-fidelity algorithm, we explore reduced-order modeling for the rotor to provide an alternative to the fully modeled rotor.

Validations of the CFD simulations using the data from MTB experiments were performed using the high-performance computing resources at the NASA Advanced Supercomputing (NAS) facility at NASA Ames Research Center. Both the higher-order and the reduced-order models are available in the OVERFLOW [4] code. The reduced-order model significantly reduces the complexity of the simulations. The rotors and the propellers are modeled as infinitely thin disks, which are represented by the momentum source terms in the governing Navier-Stokes equations. The recent version of the OVERFLOW [4] code included this disk model. A detailed description of this modeling capability can be found in Ref. [5]. The full-rotor models are loosely coupled with the CAMRAD II [6] comprehensive rotorcraft analysis software and tested on various rotor systems. The current effort introduced a rotor trim algorithm. With this CAMRAD II - OVERFLOW CFD solution, the experimental investigators can adjust the rotor parameters, (e.g., the rotor pitch). The trim algorithm can eventually help construct a more detailed test matrix for future experiments.

The main objectives of this study are to validate the computational results for MTB by comparing to the experimental data, understand the interaction between flow among different structures in the tunnel, and observe rotor-rotor interference effects. Section 1 summarizes the computational model for the rotor. Sections 2-3 describe the CFD/CSD coupling. Section 4 briefly describes the experimental setup. Section 5 details the computational model that includes the wind tunnel geometry. Finally, in section 6, validation cases and some representative results with single and multiple rotors for forward flight and hover are presented. The results attempt to quantify some

aspect of the interactional effects of the support structures by interpreting the mean flow. Some instantaneous flow fields are presented that will be useful for the MTB experimental designs.

## 1. Computational Rotor Model

The helicopter flowfield was computed using the Navier-Stokes equations in two ways. The first approach used the high-fidelity full-rotor (i.e., each blade modeled) unsteady flows with moving grids. The flowfield in the second approach used a reduced-order model using a series of approximations. The first level of approximation consisted of retaining an unsteady framework and projecting the actual blades onto the disk so that they acted on the fluid as they rotate about the rotor axis. For the helicopter problem, the unsteady formulation at least captures the first harmonic effect. A further simplification was based on a steady-state assumption whereby the disk area is filled with an infinite number of blades, and the force distribution is scaled according to the trim target. In this case, the unsteady description is lost, but computational costs are drastically reduced to one steady-state simulation. The details are given in Ref. [3] and the solved equations are shown below. The rotor is modeled as a disk as shown in Eq.1. The source term was computed using the Blade Element Theory (BET), where the blade was represented with a series of 2-D blade sections. At each time step of the simulation procedure, at each elemental area on the rotor disk, an average of the flow properties was derived from the most recently computed Navier-Stokes solution of the flowfield. The source term was added to the Right Hand Side (RHS) of the equation, as shown in Eq (1).

$$\frac{\partial U}{\partial t} + \frac{\partial F}{\partial x} + \frac{\partial G}{\partial y} + \frac{\partial H}{\partial z} = S \qquad (1)$$

$U = [\rho, \rho u, \rho v, \rho w, \rho E]^T$ is the vectors of conservative variables. $F, G, H$ are the convective and diffusive flux tensors in x, y, z. $S$ is the formal introduction of the source terms due to the actuator disk (force per unit area of the disk)

$$f = (f_x, f_y, f_z)$$
$$S = [0, f_x, f_y, f_z, (f \cdot v)]^T$$

The effect of blade motions and deformations, namely pitching and flapping degrees of freedom were determined based on the rotor trim. Torsional deformations were not included in the simulation presented here, though the coupled interface has the option to include the torsion deformations. A simplified trim procedure for the target thrust and moment balance is available in OVERFLOW. The appropriate approach, however, is to loosely couple OVERFLOW to CAMRAD II. CAMRAD II is a comprehensive analysis of rotorcraft that includes an aerodynamics module and structural analysis modules. CAMRAD II incorporates a combination of advanced technologies, including multibody dynamics, nonlinear finite elements, and rotorcraft aerodynamics. Figure 1 shows the iterative approach for the coupled computation, with the CSD analysis provided by CAMRAD II.
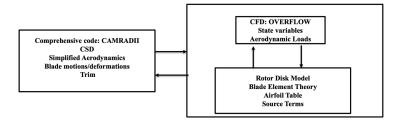


**Figure 1.** Schematic for CFD/CSD coupling for rotor disk model

## 2. CFD/CSD Coupling and Trim

CAMRAD II is interfaced with OVERFLOW for the full rotor unsteady simulation. In CAMRADII, each rotor blade is structurally modeled. Besides CSD, CAMRAD II provides full helicopter trim capability. Like the full rotor simulation, the CFD load is transferred to CAMRAD II through an interface module "delta load". The delta load between CFD and CAMRAD II is used in correcting CAMRAD II's aerodynamic load to compute new

aerodynamic data and trim. The trim procedure is an important aspect of helicopter flight where the rotor loading accounts for a significant portion of the total vehicle forces and moments. The trim task finds the equilibrium solution for a steady-state operating condition and solves performance, loads, and vibration.

Recently, CAMRAD II has been interfaced with the rotor disk model in OVERFLOW [4], including the trim capability, like the full rotor simulation. The concept of motion interface as discussed above is modified to accommodate the blade motions through control angles instead of quarter-chord displacement data in the full rotor simulation. At some specified iteration step, the CFD provides the same loads as a full rotor simulation to CAMRADII through the 'delta load' and in turn, CAMRAD II provides the trimmed angles. This procedure is described in Ref. [5]. In a typically coupled simulation, the initial execution of the CFD code is carried out for one or two complete rotor revolutions, using blade deformations from a trimmed CAMRAD II solution with the unmodified lifting-line model in aerodynamics. In subsequent coupling cycles, the flow solver is run for some n-blade multiple of a revolution between coupling cycles (full revolution for some cases), 'n' being the number of blades of a rotor. At each coupling step, rotor loads from CFD are provided to CAMRAD II and in turn, CAMRAD II uses this CFD load to correct its lifting-line aerodynamics to retrim the rotor. At convergence, the CFD airloads fully replace comprehensive analysis airloads.

## 3. Experimental Setup

A detailed description of the experiment of the Multirotor Test Bed (MTB) project is given in Refs. [1-2]. Figure 2 shows the MTB as it was tested in the U.S. Army 7- by 10- Foot Wind Tunnel at NASA Ames Research Center. The MTB has the flexibility to test larger-scale rotor configurations when compared to previous tests using small hobby-scale Urban Aircraft System (UAS). This allows for testing at rotor tip Reynolds numbers more relevant to full-scale piloted electric Vertical Take-Off and Landing (eVTOL) aircraft expected for UAM operations. The experiment allows the multirotor design space to be parametrically explored. By measuring individual rotor loads for a multirotor system and allowing for adjustments to individual rotor position and tilt angle. Each rotor can tilt forward 90 deg and backward 5 deg about the hinge. In addition, the entire MTB can tilt forward 20 deg and backward 10 deg through the central support structure, known as the strongback. The strongback is the backbone of the support structure assembly. The flexibility of the strongback assembly allows the entire multi-rotor system to be tested in many different multirotor and tilting-rotor configurations. The rotors can be arranged in tall and short configurations height-wise via adjustable support arms. The CFD simulations will be validated for the multirotor configurations in hover and edgewise forward flight for short configurations in this work.
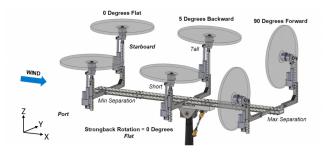


**Figure 2.** The left MTB in the U.S. Army's 7-by 10-Foot Wind Tunnel at NASA Ames Research Center[1,2]. Picture on the right shows the tall and short configuration of the rotor support arms.

## 4. Overset Grid System

The overset grid system used in the present simulation was generated using the Chimera Grid Tools (CGT) software [7]. CGT contains a very efficient and modular grid scripting library used for grid manipulation, generation, reorganization, overset hole cutting surfaces, and generation of OVERFLOW input files. This scripting procedure produces high-quality surface grids and subsequent volume grids with a set of input parameters. These parameters allow the grid system to be quickly and automatically modified for the existing geometry. Figure 3 shows the computational model for the modified MTB structure inside the tunnel. For the tunnel wall computational geometry, the tunnel test section is represented exactly and is extruded at the entrance and the exit. At the entrance, is extended about half of the tunnel test section length and at the exit about one tunnel length.
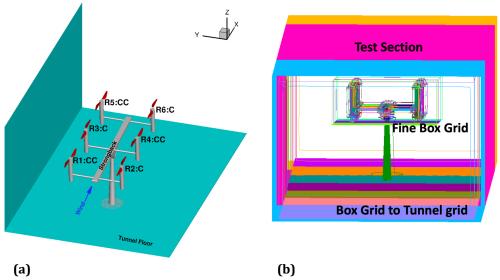
3

|  (a)  |  (b)  |

**Figure 3.** (a). Computational domain showing rotor numbering and configuration. C-clockwise, CC-counterclockwise rotor. (b). Right picture shows volume mesh that transitioned to the wall grid.

**4.1 Rotor Geometry**

The MTB uses six KDE-CF245-DP two-bladed, 24.5in., carbon fiber rotors. The blades were 3D-scanned to generate an accurate three-dimensional geometry, which provides camber, thickness, chord, and twist characteristics. Twenty-five airfoil sections were identified along the span to provide accurate blade characteristics for use in the simulations. The KDE-CF245-DP airfoil sections of the rotor blade, and radial location are shown in Table 1. Besides the computational grid for the full blade simulation, the airfoil table plays a very important role in implementing a more accurate rotor-disk model.

| r/R | Airfoils | KDE-CF245-DP Airfoil Sections |
|-----|----------|-------------------------------|
| 0.1891 | KDE1 | MTB_roR_1891.c81 |
| 0.2662 | KDE2 | MTB_roR_2662.c81 |
| 0.7515 | KDE3 | MTB_roR_7515.c81 |
| 0.9435 | KDE4 | MTB_roR_9435.c81 |

**Table 1.** Radial locations of KDE-CF245-DP Airfoil Sections

Airfoil tables are generally created using two-dimensional (2D) computational analyses of an airfoil shape for a specified range of angle-of-attack and Mach number pairs or by wind tunnel testing. The 2D analysis computes the section lift coefficients, drag coefficients, and moment coefficients. There are two approaches to determine the lift and drag of the blade elements. The first and widely used approach is to use airfoil tables arranged in the C81 format. Coefficients for airfoil lift, drag, and pitching moment are listed as a function of Mach number and angle-of-attack. The main geometric characteristics of the rotor blades [1] are summarized in Table 2. Figure 4 shows the non-linear blade twist and chord distribution.

| Rotor Parameters | Values |
|------------------|--------|
| Radius, R | 12.125 inch |
| Number of Blades, $N_b$ | 2 |
| Geometric Solidity | 0.08460 |
| Mean Chord, $C_{mean}$ | 1.3566 inch |

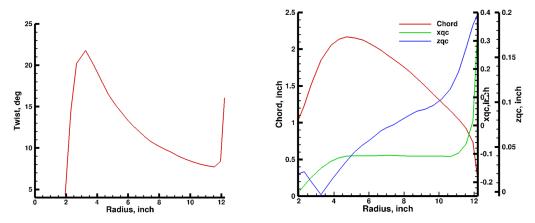**Table 2.** Geometric Properties of the Rotor.

4

**Figure 4.** Geometric properties: Blade Twist, Chord, and Quarter-chord distribution

Figure 5 (a) shows the blade planform as provided by Refs [1-2] and the computational grid for the rotor. The O-grid system used in the present simulations is shown in Fig. 5 (b). The blade tip geometry is accurately represented in the surface grid, including all sharp edges. The overset grids for each rotor blade consist of three separate grids: the main rotor-blade body, a cap grid at the outboard tip, and a cap grid at the inboard root. The main rotor-blade body uses an O-mesh topology that maintains good surface resolution. The viscous spacing provides an average $y^+$ of approximately 1.0 or less. For the rotor-disk model the cylindrical grid system used is shown in Figure 6 (a). Figure 6 (b) shows a cutout view of the grid with the representative disk plane for the source terms and the indices that are used in the OVERFLOW rotor-disk algorithm. For both grid systems, the "Near-Body (NB)" grids refer to the curvilinear overset surface grids of the rotor, tunnel, and support structures. These are embedded into a Cartesian Off-Body (OB) box grid which fills the tunnel space by resolving the rotor wake region and extending the computational domain to the tunnel wall grid. These off-body Cartesian box grids are generated within OVERFLOW according to user-specified input parameters and at various levels of resolution starting from Level 1 (L1) in the rotor-wake region, to successively coarser grid levels (L2, L3, L4…etc.) to extend the grid system rapidly and efficiently fill out the tunnel as well as beyond the test section. For this study, the box grid spacing is constant and two different resolution was used in this study. Detailed grid statistics are shown in Table 3 in section 5.
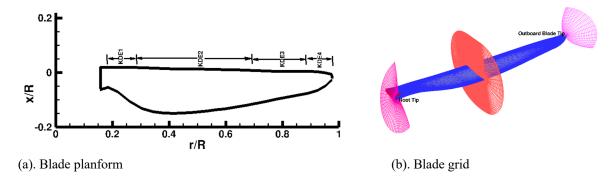


(a). Blade planform             (b). Blade grid

**Figure 5**. (a). Schematic of blade planform. (b). Blade grid

(a). Disk with block grid at singular axis          (b). Grid indices used in source term
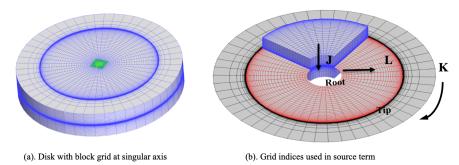
**Figure 6**. Grid used in the rotor disk model.

## 5. Computational Approach

Details of the various aspects of the OVERFLOW algorithms are available in many publications including Ref. 4. A brief description of the CAMRAD II comprehensive code, the fluid/structure loose coupling procedure, the UH-60A geometry, the overset grids, and the OVERFLOW CFD code are described in this section.

### 5.1 Comprehensive Analysis and Rotor Trim

The rotorcraft CSD code used for this study is CAMRAD II [6]. The aerodynamics modules within CAMRAD II are based on lifting-line models utilizing airfoil tables, coupled with wake models. Within CAMRAD II, each blade is structurally modeled as a set of nonlinear beam elements. In addition to the structural dynamics modeling, CAMRAD II offers a trim capability. For the UH-60A simulations in this paper, a three degree-of-freedom trim was utilized, with the solidity-weighted thrust coefficient, pitching moment, and rolling moment specified as trim targets within CAMRAD II. In turn, CAMRAD II provides the collective pitch, longitudinal cyclic, and lateral cyclic pitch angles. The details of this comprehensive code and coupling strategies are described in Ref. [4-5].

### 5.2 Flow Solver Algorithm

OVERFLOW is a high-fidelity finite-difference, overset grid, RANS CFD code. Besides the higher-fidelity, OVERFLOW recently implemented a reduced-order rotor-disk model, Ref [4]. The reduced-order method using a rotor-disk model in the OVERFLOW CFD code is one of the important aspects of this study. For these multi-fidelity algorithms, user-supplied, body-fitted structured grids are employed near solid surfaces, with automatically generated background Cartesian grids filling the remainder of the computational domain. Higher-order spatial differences for convective fluxes with $5^{th}$ order accuracy on uniform Cartesian grids are available. The code has several upwind flux schemes to improve the numerical accuracy for high-speed applications as well as for vortex-dominated flows. The results presented here were obtained using one of the HLL [8] family of upwind approximate Riemann flux algorithms, namely, the contact preserving HLLC [9] variant, with nominally 5th order WENO reconstruction for the inviscid fluxes. To advance the solution in time, an implicit, second-order backward difference scheme is used in which the nonlinear system of equations is linearized at each time step. In this study, the resulting system of linear equations is solved using symmetric successive overrelaxation (SSOR) [10], which eliminates factorization errors at the expense of more computational work and memory per time step. Within OVERFLOW, several time-stepping schemes are available, including dual-time schemes. This study used the Newton iteration scheme. For this simulation, OVERFLOW used anywhere from 10 to 40 subiterations at each time step. Several turbulence models are available in OVERFLOW. Here, the standard one-equation model of Spalart-Allmaras [11] with Detached Eddy Simulation (DES) [12] length scale models were utilized.

## 6. Results for MTB in forward flight: short configuration

Computations have been performed, including validation and a verification showing the convergence and effectiveness of the interface between OVERFLOW and CAMRAD II. These results include a wide range of configurations from single to multiple rotors and from a conventional helicopter to UAM concept vehicles. The MTB wind tunnel experiment demonstrated all the capabilities of testing with 1, 2, 4, and 6 rotors, tilting the rotors, pitching the whole model, moving the rotors in different positions/configurations, and testing at wind

tunnel speeds of 0, 20, and 40 ft/s. The computational simulations here attempted to demonstrate most of the experimental tests.

Before comparing the computational and experimental results, a flow visualization is presented in Figure 7 for the six-rotor case with support structure assembly pitched at -5 degrees. The results shown in Figure 7 are for the full blade simulations of Overflow. The MTB flowfield is complex. The vortex evolution shows the growth structure, wandering, turbulence merging, and somewhat complex merging with the shear layer and with tip vortices from other blades, and rotor-structure interactions. The shear layer leaving the blade and the vortex evolution are interdependent. The wake interactions with structures are higher for these low-Reynolds number flows, where the tip vortices are weaker, and the slow-moving vortices are more pronounced to velocities induced by flows due to the close proximities of the structures and the other rotors. This behavior is stronger for the aft set of rotors. One purpose of this paper is to assess the prediction capability of the solver for such complex flows.
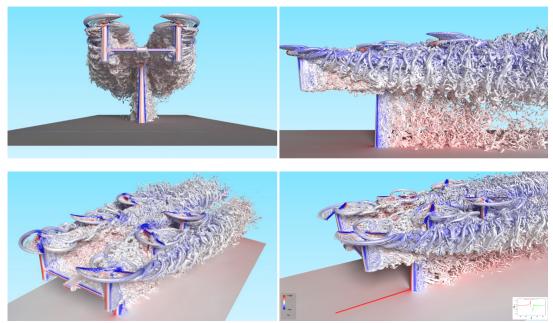


**Figure 7.** Vortices visualized with Q-criteria colored by pressure coefficient, Cp for MTB 6 rotors in Forward Flight, 40 fps, -5 deg pitch assembly. Looking at the flow with different perspectives.

Previously, slightly different verifications were performed for similar computations in refs [13] for a wind tunnel experiment. A limited verification procedure was performed to assess solution sensitivity to spatial resolution, temporal resolution including the number of subiterations used at each time step, the CFD/CSD loose coupling frequency, for a single UH-60 helicopter is provided in ref [13]. A series of runs (steps 1-6 listed below) were performed to determine an optimum choice of parameters for computation. For, subiterations, time step, and loose coupling frequency, step 3-6 we followed the guidelines suggested in ref [12] and not repeated here.

1. Spatial variations: $\{h_{i=1,3}, \Delta t, S, LC, Tr\}$: $h_{i=1,3} = $ 0.00129,0.00136,0.00145, $h$ is the grid spacing defined below, $\Delta t$ is the time step, S is the sub-iterations, LC is the loose coupling step, $Tr$ is the trim strategy.
2. Trim strategy, Tr: $\{h, \Delta t, S, LC, Tr_{i=1,5}\}$:
   1: no trim only fixed collective used in the measurement
   2: only one front rotor
   3: all 6 rotors
   4: longitudinal line rotors, rotor 1,3,5 or 2,4,6 (for rotor number refer to Figure 7 below)
   5: counterclockwise and clockwise rotors: 1,4,5 and 2,3,6 respectively
3. Subiterations S: 12-15
4. *Time step*: $\Delta t$ is equivalent to an incremental azimuthal advance $\Delta \psi$
   in degrees per physical time step. $\Delta t \ or \ \Delta \psi \ of$ 0.25 $deg$

5.  LC step: Periodic fraction based on number of blades in a rotor for full rotor simulation, 100 to 200 steps for steady state rotor disk simulation.
6.  Turbulence model sensitivity

Computations were performed for spatial sensitivity and trim strategy. For various trimming options, we presented the results for trimming 3 rotors for now. For spatial sensitivity, we use 3 different grid resolutions with the following combinations of spatial variations shown in Table 4. This parameter set provides reasonable information for making choices for numeric in practical simulations with some convergence measure. A function or a functional can be used to assess the sensitivity of the results for this convergence measure. For this validation and verification, convergence measures based on one functional of airload, $F(\psi, r) = M^2 C_n$ is used.
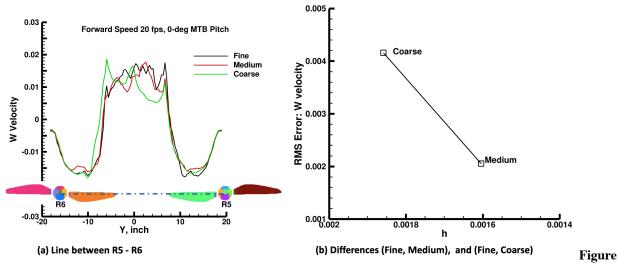
## A. Spatial Sensitivity Analysis

The near-body mesh of MTB structures and the rotors are of adequate resolutions. Further refining of the near-body grids does not change the rotor performance numbers. However, due to the different amounts and different types of numerical dissipation contained in each scheme, the structures, and the growth of eddies in the wake are highly grid size and scheme dependent. The grid refinement study was done only for the background intermediate mesh that fills the tunnel space. These intermediate box grids are referred to as L1 and L2 meshes. The refinement ratios between the two box grids were not kept fixed to avoid incompatible resolutions. Table 3 shows the details of these grids. Spatial errors are represented in a global measure of average grid spacing $h$, where $h$ = 1/ *(Total grid points)$^{1/3}$*.

Figure 8(a) shows W-velocity profile at a location at the two aft rotors where the flow interactions are high. This profile is taken at a line in the grid system through rotor hub centers of Rotor 5 and Rotor 6. The coarse grid solution changes quite a bit near the Rotor 6. The solution for all the grids is not symmetric. There are some differences although not so significant between fine and medium grid solution. Fig. 8 (b) shows the error estimate between fine mesh and the other meshes. The W-velocity shows very little differences at a location at Rotor 1 - Rotor 2, and Rotor 3 - Rotor 4 as shown in Figure 9.

Figure 10 shows normal loads for various grids for only two rotors, one front rotor R1 and one aft rotor R6. There are no significant differences between all grid system for the surface quantity, the rotor sectional load, $M^2 C_n$. The aft Rotor 6 shows slight differences toward the blade tip showing some interference effect on the surface quantities.

| Grid | Total number of grids | Total points in NB grids in millions | Total points in NB support grids in millions | Total Points in Tunnel Wall Grids in millions | Total Points in millions | Average Grid Spacing, h | Refinement Ratio |
|------|------|------|------|------|------|------|------|
| Fine | 236 | 40 | 27 | 27 | 584 | $h_1$ = 0.00119 | |
| Medium | 236 | 40 | 27 | 27 | 242 | $h_2$ = 0.00160 | $r_{21}$=$\frac{h_2}{h_1}$ = 1.34 |
| Coarse | 236 | 40 | 27 | 27 | 156 | $h_3$ = 0.00186 | $r_{32}$=$\frac{h_3}{h_2}$ = 1.16 |

**Table 4.** Spatial sensitivity analysis with various grids, 6-Rotor, Tunnel Speed = 20 fps, MTB Pitch = 0 deg,

**Figure 8.** Spatial sensitivity analysis with various grids, 6-Rotor, Tunnel Speed = 20 fps, MTB Pitch = 0 deg. (a). W-velocity profile at a lateral location in at the aftmost rotors. (b). RMS difference between fine mesh and other two meshes.
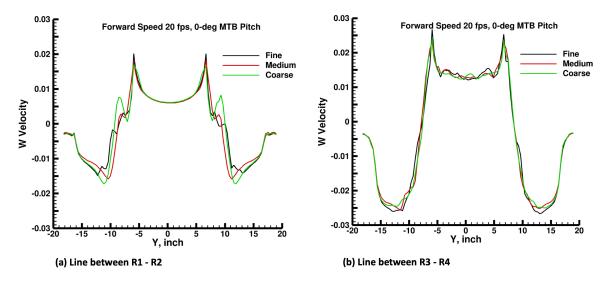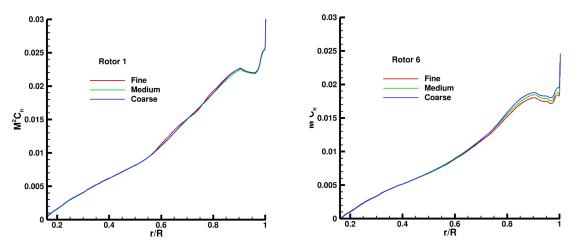


**Figure 9.** Spatial sensitivity analysis with various grids, 6-Rotor, Tunnel Speed = 20 fps, MTB Pitch = 0 deg. (a). W-velocity profile at a lateral location in at the front two rotors. (b). W-velocity profile at a lateral location in at the middle two rotors.

9

**Figure 10.** Spatial sensitivity analysis with various grids, 6-Rotor, Tunnel Speed = 20 fps, MTB Pitch = 0 deg. Sectional loads (a). at a representative front rotor, (b). at an aftmost rotor.

## B.   Trim sensitivity

In the multirotor framework, the trim strategy is an important aspect of the computation and even more so for this MTB simulation as the measurement did not maintain natural lateral symmetry. Measurements were done for configurations of 1, 2, 4, and 6 rotors. For all configurations, the simulation trims each rotor to its measured thrust. The six-rotor configurations in this study incorporated different trim strategies, namely, trim all six rotors or trim only three symmetric rotors. The differences in trimmed collective values will reflect asymmetry of wind tunnel flow if any and rotor-rotor interference. Trimming all six rotors is not necessary as the system is over-constrained and would not be allowed to maintain natural symmetry. Figure 11 shows the comparison of different trimmed strategies, trimming all six rotors versus trimming three rotors. The three-rotor trim is performed for a longitudinal row of rotors on one side, namely Y- side here (port side). It is interesting to note that the experimental thrust measurement shows a trend where Y+ side is consistently smaller in magnitude. Figure 11(a) shows the thrust whereas 11(b) shows the power requirement for the rotors. Adjusting collectives based on trimming six rotors or three rotors show negligible changes in power predictions. Here the six-rotor trim reduces the total Thrust (T)/Power (P) ratios by about 0.3 percent. The remaining forward flight results are based on the trimming of three rotors or for fixed collectives as in the experiment.
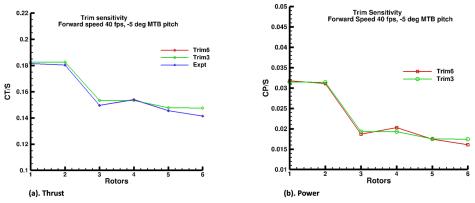


**Figure 11.** Trim sensitivity analysis with two methods, all 6-Rotors, and three longitudinal rotors on one side (right or Y- side), Tunnel Speed = 40 ft/s, MTB Pitch = -5 deg.

The six-rotor case with the rotor-disk model is shown first in Figures 12-14. Two studies were performed for the MTB's short rotor configuration for wind tunnel speeds of 20 ft/s and 40 ft/s. Figure 12

qualitatively compares the normal force, for all the rotor disks. The two varying fidelity simulations seem to be close to each other with slight changes in the magnitude and phases. In general, the disk model predicts a higher normal load on the advancing side. Nevertheless, the similarity between these two varying fidelities is encouraging. Figure 13(a, b) shows the two cases of six-rotor trimmed solutions and comparisons to the experiment. The figure on the left is -5 deg MTB pitch, while the figure on the right is 0 deg pitch MTB assembly and at a tunnel speed of 40 ft/sec. For these results, only three longitudinal rotors on one side, right side, (or Y+ side, starboard side), namely, R1, R3, and R5 were trimmed, whereas in Figure 9(b) in the sensitivity study section, the trimming was performed for the left side (Y- side, port side) rotors, R2, R4, R6. The computation preserves the lateral symmetry while the measured data show asymmetry. Figure 14 shows the convergence of the loosely coupled solution for the two front rotors. All the rotors behave similarly, so for conciseness, we presented one clockwise rotor (Rotor 2) and one counterclockwise rotor (Rotor 1). CII in these figures refers to comprehensive code CAMRADII while OF is referred to as OVERFLOW. At the OF and CII interface, the load is transferred through a delta module at CII collocation points. This is done in general because a higher resolution requirement on the comprehensive side is not needed as opposed to the CFD level. At 'loose coupling (LC)' convergence, this delta load should approach zero. The two plots on the left of (Fig. 14(a-b)) are the normal loads for OF and CII at the CII collocation points. They are close to each other at convergence. The right figures show the value of delta loads and L2-norm of delta load.
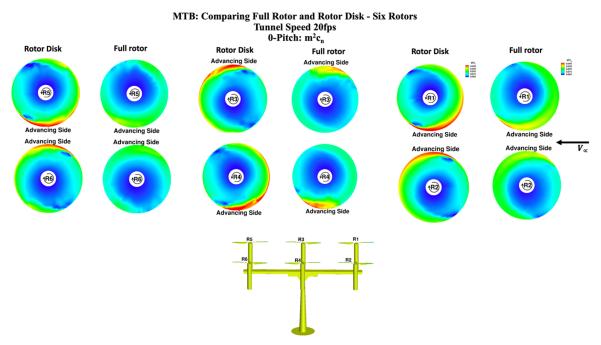


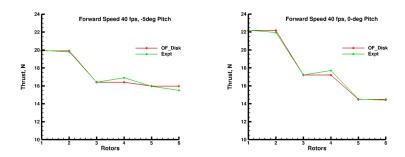**Figure 12.** MTB: $M^2 C_n$ on the disk plane. Comparing Full Rotor versus Rotor Disk Model solution for six rotors.



**Figure 13.** MTB 6 rotors: Comparing Rotor-Disk model trimmed solution to the experiment.
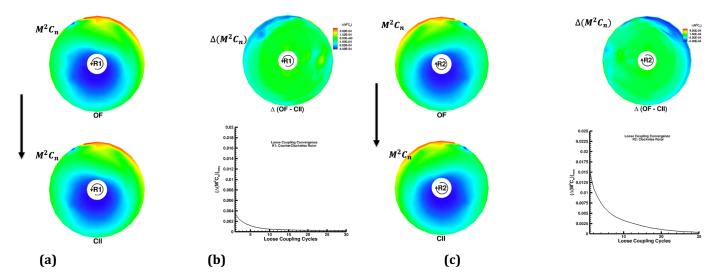
11

**Figure 14.** Loose Coupling (LC) Convergence for R1 and R2: $\{\Delta(M^2 C_n)\}_{rms} \in (LC)\{$OF and CII on CAMRAD Data point$\}$. Left two figures in (a) and (b) show the normal load at the CAMRAD collocated points. Right two figures show the delta load convergence between OVERFLOW and CAMRAD II.
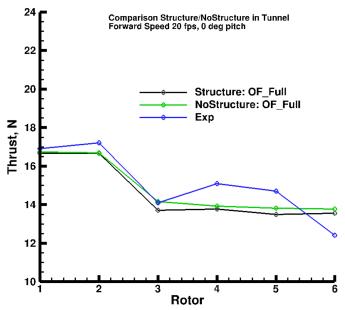


**Figure 15.** Thrust comparing simulations with/without structures inside the tunnel for a fixed collective to experimental data. MTB 6 Rotors in Forward Flight, 20 ft/s, 0-deg MTB Pitch assembly.

The support structure's interference effects are shown in Figures 15-18. Figure 15 compares simulations with experimental results for 6 rotors with fixed collective and no trimming for the MTB pitch of -5 deg and 20 ft/s tunnel speed, with and without the MTB structure inside the tunnel. Simulations maintain lateral symmetry as opposed to measurement asymmetry. In all the configurations, Ref [1-2] attributed asymmetry in the measurements to the possible load cell calibration issues or the influence of vibrations/resonances affecting the load cells unequally. This measured asymmetry is seen in all the configurations.

Figures 16 to 18 attempt to quantify the detailed effect of the support structures, and the inter-rotor interactions inside the tunnel. The first three plots of Fig. 16(a-c) show the sectional normal forces at a radial station of r/R= 0.865. Figure 16(d) shows the radial normal forces. The normal forces for front two rotors in

12

both cases show very little changes in the magnitude although there seems to be a constant phase shift. For the middle and aft rotors, there are changes in the magnitude as well. The in-plane multirotor arrangement appears to dominate for many UAM configurations, and it would be interesting to look at the velocity and pressure field. The velocity profiles are shown for both longitudinal and lateral rotors. All these cases are for the 6-rotor configuration in forward flight, 20 ft/s, and 0-deg MTB pitch.

In Figures 17 and 18, the basic component of the in-plane multirotor wakes, velocity profiles, and pressure coefficients are depicted. The mean velocity and pressure fields presented here were obtained after averaging one rotor revolution of instantaneous velocity fields (about 360 instantaneous velocity fields). In these figures, schematics of the velocity and pressure profile locations are shown. The bottom schematics in each plot show how the W-velocity profiles relate to the location of the rotors. Figure 17 contains plots of velocity profiles extracted at the longitudinal and lateral locations in the rotor plane. These profiles are taken from hub center to hub center. The longitudinal profile is taken from the hub of Rotor 1, through Rotor 2, and to the inline aft hub of Rotor 5. The lateral profiles are for each symmetric rotor pair. These velocity profiles are useful in estimating contributions of different sections of rotor disk in generating thrust. The maximum changes occur at approximately 0.90 r/R as is consistent with the radial force profile in Fig. 14(c). For the lateral profiles, the front two rotors show very little changes in the velocity profile except for the sharp changes in the velocities for the case of the rotor with structures. In general, the aft rotors, for both the longitudinal and lateral profiles, show some variation in the velocities for the two cases of structure versus no structures inside the tunnel, especially near the main support strut. The velocity profile near the main support strut shows a significant upward directed flow.

Figure 18 presents the pressure variation along tunnel wall, ceiling, and the tunnel floor, and at an outflow location below the rotor hub. The pressure variation is shown for the rotor configurations with and without the structures inside the tunnel. Wide changes in pressures at the location near the middle rotors to the aft rotors. Fig. 18(c-d) quantifies the pressure differences. The floor pressure changes are minimal except near the main support strut, where flow separation and the Karman vortex street is dominant. The pressure changes at the location below the hub are noticeable. Investigation of the power requirement shows the effect of the structure-rotor interactions. The power prediction was shown previously in the trim sensitivity section. The structure/no structure effect on the tunnel wall pressures are shown Fig. 16. These pressures are shown along the three lines on the wall as indicated in the figures on the bottom right of the plots. The structure has more effects on the four aft rotors, especially, the middle two rotors as seen in the pressure variation on the tunnel floor line. The wall effect seems to be negligible due to the side walls as Cp variation is minimal. In general, the tunnel effect is not negligible for multirotor configurations.
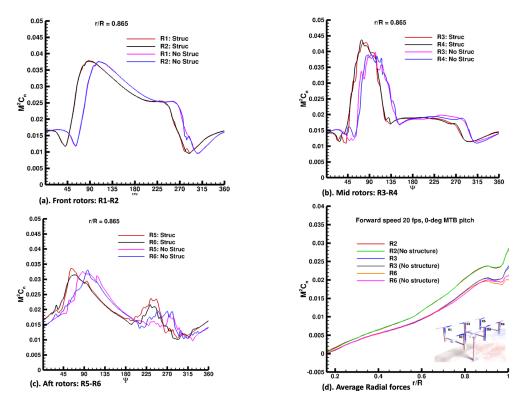
**Figure 16.** Sectional normal force coefficient showing the effect of support structures and body inside the tunnel.
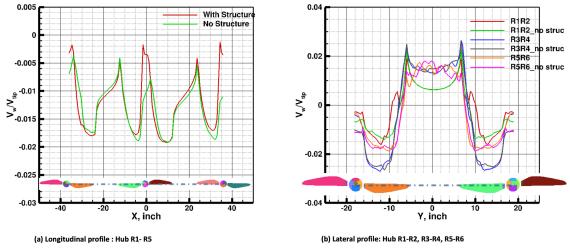


**Figure 17.** Velocity profiles showing the effect of support structures and body inside the tunnel. MTB 6-rotor, tunnel speed 5fps, 0-deg MTB pitch.

Figure 19 compares simulation results with the experimental data for 4 rotors with fixed collective and no trimming. This simulation modeled the four-rotor short configuration, rotors R1, R2, R3, and R4, for a MTB pitch of -5 deg and at 20 ft/s tunnel speed.

Table 5 and Figure 20 compares the two rotor cases with fixed collective. In the experiment, for the two-rotor study cases, rotors 3 and 4 were used for -10, -5, and 0 deg MTB pitch angle, at 20 ft/s tunnel speed, in the short rotor configuration. For this simulation, a MTB pitch of -5 deg is used. The disk model over-predicts

14

the thrust values while the full rotor underpredicts. Figure 20 presents the particle traces colored with Cp. The particles are released from the front. Small interactions are noticeable at the support structures.
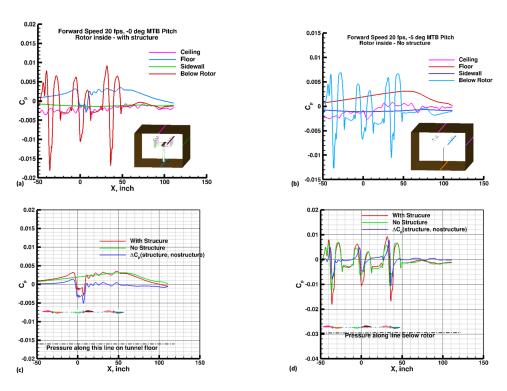


**Figure 18**: Pressure profiles at different locations at the tunnel walls, tunnel floor, and longitudinal line below the rotors. (a) Rotor with full structure, (b) Isolated rotors with no structure in the tunnel, (c) Pressure difference at floor – structure/no structure, (d) Pressure difference at a location below rotor: structure/no structure. MTB 6-rotor, tunnel speed 5fps, 0-deg MTB pitch.
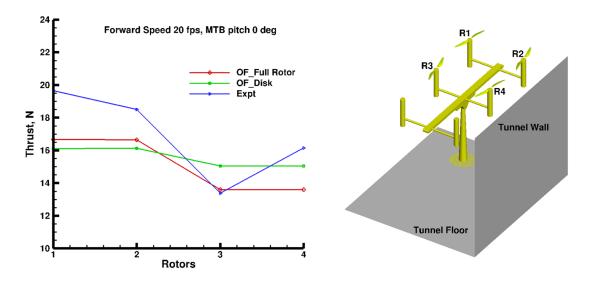


**Figure 19.** MTB 4 rotors: Comparing Rotor-Disk Solution to the experiment. 20 fps, 0-deg MTB Pitch assembly.

| Rotors | OF_Full Thrust, N | OF_Disk Thrust, N | Expt. Thrust, N |
|---|---|---|---|
| 3 | 16.20 | 18.90 | 16.9 |
| 4 | 16.17 | 18.90 | 17.8 |

**Table 5.** MTB 2 rotors: Comparing Rotor-Disk solution to the experiment. 20 fps, 0-deg MTB Pitch assembly.
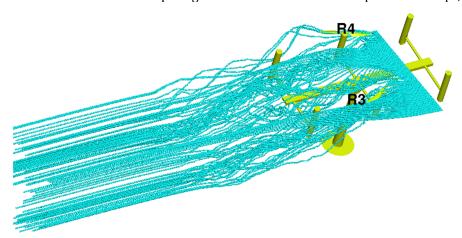


**Figure 20.** MTB 2 rotors: Comparing Rotor-Disk solution to the experiment. 20 fps, 0-deg MTB Pitch assembly.

Finally, hover results for a single rotor are presented. A simple isolated rotor, Rotor 2 was tested in the tunnel. Table 6 compares the Figure of Merit (FM) of the rotor for the full rotor simulation, disk model simulation, and the experimental data. The disk model FM prediction seems to match the measured values well as opposed to the under prediction for the full rotor simulation. Figure 21 shows the cut-away view of the vortex wake, where the particle traces were colored with vorticity magnitude. The current grid system shows the well-resolved turbulent structures. Figure 22 shows a full view of the hover flow field for both the full rotor as well as for the rotor disk model simulations. The particle traces here are colored by pressure coefficient. Even for this small-scale rotor system, from this flow visualization it is evident that the rotor blade vortices are a dominant feature in the turbulent rotor wake as they are initially formed at a blade tip by the roll-up of the blade trailing edge shear layer. The rotor trailing edge wake shear layers contain vorticity that is initially formed on the rotor blades. Beside these shear layer vorticity is stretched and elongated as it is entrained into the vortex, they also have interferences the support structures, especially the vertical support. Some quantification of the interference, however small that may be shown for forward flight above.

| Cases | FM |
|---|---|
| FM: Full Rotor | 0.710 |
| FM: Disk | 0.713 |
| FM: Expt | 0.714 |

**Table 6.** Isolated Rotor (Rotor 2) in Hover, comparing FM
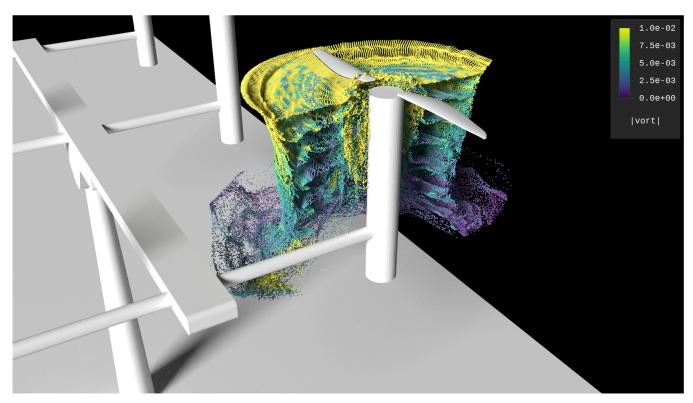
**Figure 21.** Isolated Rotor (Rotor 2) in Hover. Cut-away view of the vortex wake.



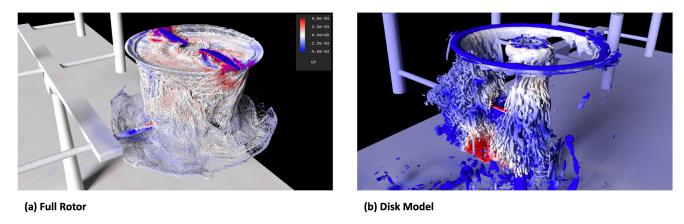**(a) Full Rotor**                                    **(b) Disk Model**

**Figure 22.** Isolated Rotor (Rotor 2) in Hover. Particle traces showing Cp.

**Summary and Future work**

    MTB simulations using OVERFLOW Navier-Stokes computation with both the time-accurate and rotor-disk steady-state analysis are presented for various rotor configurations in forward flight as well as for hover. The computational details and methodology were summarized, and some of the details of this study are mentioned below:

1.  The grid generation was based on an initial CAD model of the various support structures inside the tunnel. The tunnel geometry was not part of the CAD model. However, an attempt will soon be made to use the latest CGT auto-gridding tool, provided the CAD model of the tunnel is available.
2.  A limited verification procedure was performed to assess solution sensitivity to spatial resolution, and different trim strategies for multirotor configurations. For spatial sensitivity, grid refinement was performed only for the intermediate box grids that fills the tunnel space.

17

3. The rotor disk results were presented for a loosely coupled comprehensive code CAMRAD II for a few of the configurations inside the tunnel. The computational details were compared with wind tunnel measured data. The analyses and experimental setup are briefly discussed.
4. Both qualitative and quantitative comparisons of the computed and measured flow field reveal that the simulation captures the key features of the complex rotor wake, rotor-structures interactions, and rotor-rotor interactions. However, in the case of fixed collective setting of the experiment, the computed thrusts agree with the measured trends within a reasonable bound except for the lateral symmetry. Computation maintains lateral symmetry for all the configurations as opposed to the measured thrust.
5. Most of the qualitative comparisons are done with fixed rotor collectives. For different collective settings, some aspects of the rotor trimming were performed with the rotor-disk algorithm. As mentioned before, the trim sensitivity studies were performed. This may help MTB measurements to adjust the rotor parameters more precisely and in new ways, especially the rotor pitch. The trim algorithm can eventually be used to help prepare a more detailed test matrix as well. The rotor trim would help the power prediction appropriately.
6. The experimental thrust measurement shows a trend where Y+ side is consistently smaller in magnitude. Reasons for this are unclear and are continuing to be investigated.
7. The interactional dynamics between rotor-rotor and rotor-structures are presented and are reflected in power requirement results. The influence of structures is presented with some quantification.
8. The basic component of the in-plane multirotor wakes and velocity profiles are identified and discussed.
9. Future work seeks to observe the effects of out-of-plane rotor configurations as well as the parametric studies of the rotor proximity distance changes.

**Acknowledgements**

**References**

1. Russell, C. and Conley, S., *The Multirotor Test Bed – A New NASA Test Capability for Advanced VTOL Rotorcraft Configurations*, Vertical Flight Society 76th Annual Forum and Technology Display, October 6-8, 2020
2. Conley, S., Russell, C., Kallstrom, K., Koning, W., and Romander, E., *Comparing RotCFD Predictions of the Multirotor Test Bed with Experimental Results*, Vertical Flight Society 76th Annual Forum and Technology Display, October 6-8, 2020
3. Conley, S., Shirazi, D., *Comparing Simulation Results from CHARM and RotCFD to the Multirotor Test Bed Experimental Data*, AIAA Aviation Forum, August 2-6, 2021.
4. Buning, P., *OVERFLOW 2.3b*, NASA Langley Research Center, April 2020.
5. Ahmad, J.U., *Rotor Disk Model in the OVERFLOW CFD Code with Application*, to be submitted for presentation/publications.
6. Johnson, W.R., *Technology Drivers in the Development of CAMRAD II* American Helicopter Society Aeromechanics Specialists' Meeting, San Francisco, CA, Jan. 1994.
7. Chan, W.M., *Developments in Strategies and Software Tools for Overset Structured Grid Generation and Connectivity*, AIAA paper 2011-3051, AIAA 20th Computational Fluid Dynamics Conference, Honolulu, Hawaii, June 27-30, 2011.
8. Harten, A., Lax, P. D., and van Leer, B., *On Upstream Differencing and Godunov-type Schemes for Hyperbolic Conservation Laws*, *SIAM Review,* Vol. 25, No. 1, 1983, pp. 35–61.
9. Toro, E. F., Spruce, M., and Speares, W., "Restoration of the Contact Surface in the HLL Riemann Solver," *Shock Waves,* Vol. 2, 1994, pp. 25–34.
10. Nichols, R., Trammel, R., and Buning, P., *Solver and Turbulence Model Upgrades to OVERFLOW 2 for Unsteady and High-Speed Flow Applications,* AIAA-2006-2824, June 2006.
11. Spalart, P. R., and Allmaras, S. R., "A One-Equation Turbulence Model for Aerodynamic Flows," AIAA Paper 92-0439, January 1992.
12. Spalart, P. R., Jou, W-H., Strelets, M., and Allmaras, S. R., *Comments on the Feasibility of LES for Wings and*

*on a Hybrid RANS/LES Approach,* First AFOSR Conference on DNS/LES, August 1997, Greyden Press, Columbus, OH.

13. Ahmad, J.U., Yamauchi, G.K., Kao, D.L., *Comparison of Computed and Measured Vortex Evolution for a UH-60A Rotor in Forward Flight,* AIAA-2013-3160, 31st AIAA Applied Aerodynamics Conference, 24-27 June 2013, San Diego, CA.